Numerical Modelling of Coupled Surface and Subsurface Flow Systems

Prince Chidyagwai [a] and Beatrice Rivière [a,1]

[a] *Department of Computational and Applied Mathematics, Rice University, 6100 Main Street, Houston, TX 77005, U.S.A.*

Abstract

This paper presents and compares several numerical solutions of the coupled system of Navier-Stokes and Darcy equations. The schemes are based on combinations of the finite element method and the discontinuous Galerkin method. Accuracy and robustness of the methods are investigated for heterogeneous porous media. The importance of local mass conservation for filtration problems is also discussed.

Key words: Navier-Stokes equations, Darcy's law, discontinuous Galerkin, finite element method, Beavers-Joseph-Saffman, mass conservation, fractured porous media

1 Introduction

Coupling incompressible flow and porous media flow has become an active area of research because of the wide range of applications (see for instance [1, 2, 3]). In this paper we present a general formulation of the coupled Navier-Stokes and Darcy equations. The different physical flows are coupled via appropriate transmissibility conditions that include balance of forces and the Beavers-Joseph-Saffman's law. We numerically study three algorithms that are based on the finite element method and the primal discontinuous Galerkin method. The continuous finite element method is traditionally used in computational

[1] The second author acknowledges the support of NSF through the grant DMS 0810422.

fluid dynamics. The discontinuous Galerkin method is well suited for solving flow in heterogeneous porous media because it is locally mass conservative, it can be of high order and it is easily implemented on unstructured non-conforming meshes. Throughout the text we refer to the finite element method as CG and to the discontinuous Galerkin method as DG. This work shows the optimal convergence of the proposed algorithms and compares them by determining their robustness with respect to the spatial variations of the interface, the permeability of the porous medium and the kinematic viscosity.

The coupling of Stokes and Darcy equations has been extensively studied in the literature. A non-exhaustive list of papers is [4, 5, 6, 7, 8, 9, 10, 11]. The weak formulation of the coupled Navier-Stokes and Darcy equations is proposed and analyzed in [12, 13, 14] for the steady-state case and in [15, 16] for the time-dependent case. A priori error estimates for various numerical solutions are also obtained in [13, 14, 15, 17, 16].

Let $\Omega \subset \mathbb{R}^2$ be a polygonal bounded domain that has been partitioned into several subdomains, each of which contains either a porous medium or a free flowing fluid. Let Ω_1 denote the union of all free flow regions and let Ω_2 denote the union of all porous media flow regions. The fluid velocity $\boldsymbol{u}_1$ and fluid pressure p_1 in the free flow regions satisfy the Navier-Stokes equations:

$$-2\nu\nabla\cdot(\boldsymbol{D}(\boldsymbol{u}_1)) + \boldsymbol{u}_1\cdot\nabla\boldsymbol{u}_1 + \nabla p_1 = \boldsymbol{f}_1, \quad \text{in } \Omega_1, \tag{1}$$
$$\nabla\cdot\boldsymbol{u}_1 = 0, \quad \text{in } \Omega_1, \tag{2}$$
$$\boldsymbol{u}_1 = 0, \quad \text{on } \Gamma_1. \tag{3}$$

The boundary of the Navier-Stokes region that does not include the interface $\partial\Omega_1 \cap \partial\Omega_2$ is denoted by Γ_1. The parameter $\nu > 0$ is the kinematic viscosity, the function $\boldsymbol{f}_1$ is an external force acting on the fluid, the matrix $\boldsymbol{D}(\boldsymbol{u}_1)$ is the rate of strain:

$$\boldsymbol{D}(\boldsymbol{u}_1) = \frac{1}{2}(\nabla\boldsymbol{u}_1 + (\nabla\boldsymbol{u}_1)^T). \tag{4}$$

The flow in Ω_2 is of single phase flow type and it is modelled by Darcy's law. Darcy's law is valid for creeping flow where the Reynolds number is very small, which is a physically reasonable assumption for flow in porous media. Let p_2 denote the fluid pressure in the porous media.

$$-\nabla\cdot\boldsymbol{K}\nabla p_2 = f_2, \text{ in } \Omega_2, \tag{5}$$
$$p_2 = 0, \text{ on } \Gamma_{2\mathrm{D}}, \tag{6}$$
$$\boldsymbol{K}\nabla p_2\cdot\boldsymbol{n} = g_{\mathrm{N}}, \quad \text{on } \Gamma_{2\mathrm{N}}. \tag{7}$$

The matrix $\boldsymbol{K}$ is symmetric positive definite and it is the hydraulic conductivity which depends on the properties of the fluid and the characteristics of the porous medium. The hydraulic conductivity can be written as

$$\boldsymbol{K} = \frac{\boldsymbol{k}g}{\nu},$$

where $\boldsymbol{k}$ is the intrinsic permeability and g is the acceleration constant due to gravity. The function f_2 is a body force. The Darcy velocity is directly obtained from the pressure by Darcy's law:

$$\boldsymbol{u}_2 = -\boldsymbol{K}\nabla p_2.$$

We assume that the boundary of the porous medium $\Gamma_2 = \partial\Omega_2 \cap \partial\Omega$ is the union of two disjoint sets $\Gamma_{2\mathrm{D}}$ and $\Gamma_{2\mathrm{N}}$ on which Dirichlet and Neumann boundary conditions are imposed. Thus Γ_2 does not include the interface $\partial\Omega_1 \cap \partial\Omega_2$. For simplicity, we assume that $\Gamma_{2\mathrm{D}}$ has positive measure. Otherwise we have to impose an additional constraint on the pressure such as: $\int_{\Omega_2} p_2 = 0$. The vector $\boldsymbol{n}$ denotes the unit outward normal to $\partial\Omega$.
We denote by $\Gamma_{12} = \partial\Omega_1 \cap \partial\Omega_2$ the interface between the regions Ω_1 and Ω_2. The coupling of the system of equations in (1)-(7) is completed by interface conditions, corresponding to the continuity of the normal component of velocity, the balance of forces across the interface and the Beavers-Joseph-Saffman law. We refer the reader to [18, 19] for details on the significance of these conditions. We assume the porous medium to be isotropic. In the case of anisotropic medium, the Beavers-Joseph-Saffman's law should be modified [20]. Let $\boldsymbol{n}_{12}$ be the unit normal vector to Γ_{12} directed from Ω_1 to Ω_2 and let $\boldsymbol{\tau}_{12}$ be the unit tangent vector on Γ_{12}. The interface conditions are given below.

$$\boldsymbol{u}_1 \cdot \boldsymbol{n}_{12} = -\boldsymbol{K}\nabla p_2 \cdot \boldsymbol{n}_{12}, \text{ on } \Gamma_{12}, \tag{8}$$

$$-2\nu \boldsymbol{D}(\boldsymbol{u}_1)\boldsymbol{n}_{12} \cdot \boldsymbol{n}_{12} + p_1 = p_2, \text{ on } \Gamma_{12}, \tag{9}$$

$$\alpha \boldsymbol{K}^{-1/2}\boldsymbol{u}_1 \cdot \boldsymbol{\tau}_{12} = -2\nu(\boldsymbol{D}(\boldsymbol{u}_1)\boldsymbol{n}_{12}) \cdot \boldsymbol{\tau}_{12}, \text{ on } \Gamma_{12}. \tag{10}$$

The parameter $\alpha > 0$ is obtained from experimental data. We refer the reader to [14, 13] for the existence and uniqueness of a weak solution for the coupled problem (1)-(10). Because of the nonlinearity in the momentum equation (1), a small data condition is assumed to hold throughout the paper. The small data condition says that either the input data $(\|\boldsymbol{f}_1\|_{L^2(\Omega_1)}, \|f_2\|_{L^2(\Omega_2)}, \|g_{\mathrm{N}}\|_{L^2(\Gamma_{2\mathrm{N}})})$ is small enough or the kinematic viscosity ν is large enough.

The rest of the paper is as follows. Section 2 defines three numerical algorithms for solving the model problem and states the theoretical results. Numerical convergence rates are obtained for known solutions in Section 3. Simulations of coupled flow for various heterogeneous porous media are shown in Section 4. The methods are applied to a filtration problem and numerical mass errors are computed. Finally conclusions follow.

2 Numerical Schemes

The domain Ω is subdivided into triangles such that the interface Γ_{12} is the union of whole edges. The triangulation (or mesh) $\mathcal{E}^h$ is assumed to be regular. The maximum diameter of a mesh element over all triangles is denoted by h. The mesh is finer as h decreases. We first define formally variational methods for solving the coupled model problem. We seek to find approximation $\boldsymbol{U}^h$ of the Navier-Stokes velocity, approximation P_1^h of the Navier-Stokes pressure and approximation P_2^h of the Darcy pressure in finite dimensional spaces $\boldsymbol{X}^h, Q^h, M^h$ respectively. We will define these spaces later. We introduce formally bilinear forms that correspond to various discretizations of the different operators in (1), (2) and (5). To be more precise, we make the following assumptions.

- Assume that the operator $-2\nu\nabla\cdot\boldsymbol{D}(\boldsymbol{u})$ has been discretized by a bilinear form $a_{\mathrm{NS}}:\boldsymbol{X}^h\times\boldsymbol{X}^h\to\mathbb{R}$.
- Assume that the operator ∇p has been discretized by a bilinear form $b_{\mathrm{NS}}:\boldsymbol{X}^h\times Q^h\to\mathbb{R}$.
- Assume that the operator $\boldsymbol{u}\cdot\nabla\boldsymbol{u}$ has been discretized by a trilinear form $c_{\mathrm{NS}}:\boldsymbol{X}^h\times\boldsymbol{X}^h\times\boldsymbol{X}^h\to\mathbb{R}$.
- Assume that the operator $-\nabla\cdot\boldsymbol{K}\nabla p$ has been discretized by a bilinear form $a_{\mathrm{D}}:M^h\times M^h\to\mathbb{R}$.
- Assume that the input data (body forces $\boldsymbol{f}_1$ and f_2 and boundary conditions g_{N}) are incorporated into a bilinear form $L:\boldsymbol{X}^h\times M^h\to\mathbb{R}$.

The transmissibility conditions (8)-(10) are taken into account by a form γ that is independent of the type of discretizations used.

$$\begin{aligned}\forall\boldsymbol{v},\boldsymbol{w}\in\boldsymbol{X}^h,\quad\forall q_2,t_2\in M^h,\quad\gamma(\boldsymbol{v},q_2;\boldsymbol{w},t_2)=\Big(q_2,\boldsymbol{w}\cdot\boldsymbol{n}_{12}\Big)_{\Gamma_{12}}\\+\alpha\Big(\boldsymbol{K}^{-1/2}\boldsymbol{v}\cdot\boldsymbol{\tau}_{12},\boldsymbol{w}\cdot\boldsymbol{\tau}_{12}\Big)_{\Gamma_{12}}-\Big(\boldsymbol{v}\cdot\boldsymbol{n}_{12},t_2\Big)_{\Gamma_{12}}.\end{aligned}$$

In the definition of γ, the notation $(\cdot,\cdot)_{\Gamma_{12}}$ is used for the L^2-inner product of functions defined on Γ_{12}. In general, for any domain $\mathcal{O}$, the notation $(\cdot,\cdot)_{\mathcal{O}}$ is used for the L^2-inner product of functions defined on $\mathcal{O}$.

Using the operator discretizations as "black boxes", we propose the general scheme: find $\boldsymbol{U}^h\in\boldsymbol{X}^h, P_1^h\in Q^h, P_2^h\in M^h$ such that

$$\begin{aligned}\forall\boldsymbol{v}\in\boldsymbol{X}^h,\,\forall q_2\in M^h,\quad a_{\mathrm{NS}}(\boldsymbol{U}^h,\boldsymbol{v})+b_{\mathrm{NS}}(\boldsymbol{v},P_1^h)+c_{\mathrm{NS}}(\boldsymbol{U}^h;\boldsymbol{U}^h,\boldsymbol{v})\\+a_{\mathrm{D}}(P_2^h,q_2)+\gamma(\boldsymbol{U}^h,P_2^h;\boldsymbol{v},q_2)=L(\boldsymbol{v},q_2),\qquad(11)\\\forall q_1\in Q^h,\quad b_{\mathrm{NS}}(\boldsymbol{U}^h,q_1)=0.\qquad(12)\end{aligned}$$

We linearize the scheme by using a Picard iteration starting with an initial guess $\boldsymbol{U}_0^h=\boldsymbol{0}$. We solve the coupled problem as a whole system for each iteration. Namely, for any $n \geq 0$, we find $\boldsymbol{U}_{n+1}^h \in \boldsymbol{X}^h, P_{1,n+1}^h \in Q^h, P_{2,n+1}^h \in M^h$ such that

$$\forall \boldsymbol{v} \in \boldsymbol{X}^h, \forall q_2 \in M^h, \quad a_{\mathrm{NS}}(\boldsymbol{U}_{n+1}^h, \boldsymbol{v}) + b_{\mathrm{NS}}(\boldsymbol{v}, P_{1,n+1}^h) + c_{\mathrm{NS}}(\boldsymbol{U}_n^h; \boldsymbol{U}_{n+1}^h, \boldsymbol{v})$$
$$+ a_{\mathrm{D}}(P_{2,n+1}^h, q_2) + \gamma(\boldsymbol{U}_{n+1}^h, P_{2,n+1}^h; \boldsymbol{v}, q_2) = L(\boldsymbol{v}, q_2), \tag{13}$$
$$\forall q_1 \in Q^h, \quad b_{\mathrm{NS}}(\boldsymbol{U}_{n+1}^h, q_1) = 0. \tag{14}$$

The termination criteria is $||\boldsymbol{U}_{n+1}^h - \boldsymbol{U}_n^h||_{L^2(\Omega_1)} \leq \delta$, for a given tolerance δ set by the user.

In the rest of the section, we complete the definition of the scheme (13)-(14) by explicitely describing the forms $a_{\mathrm{NS}}, b_{\mathrm{NS}}, c_{\mathrm{NS}}$ and a_{D}. We then obtain three algorithms based on the classical continuous finite element method and the primal discontinuous Galerkin method.

2.1 Continuous Galerkin finite element scheme (CG-CG)

The mesh is assumed to be conforming. Let $\boldsymbol{X}^h \subset \{\boldsymbol{v} \in (H^1(\Omega_1))^2 : \boldsymbol{v} = \boldsymbol{0} \text{ on } \Gamma_1\}$ and let $Q^h \subset L^2(\Omega_1)$ be finite-dimensional subspaces that contain continuous piecewise polynomials of a certain degree. We assume that the pair of spaces $(\boldsymbol{X}^h, Q^h)$ satisfies an inf-sup condition and that the approximation is of order k for a given positive integer k:

$$\inf_{\boldsymbol{w}_h \in \boldsymbol{X}^h} \|\boldsymbol{u} - \boldsymbol{w}_h\|_{H^1(\Omega_1)} + \inf_{q_h \in Q^h} \|p_1 - q_h\|_{L^2(\Omega_1)} = \mathcal{O}(h^k).$$

One example of such spaces is the MINI finite element spaces [21] (with order $k = 1$), in which the Navier-Stokes velocity is approximated by continuous piecewise linear functions enriched with bubble functions and the Navier-Stokes pressure by continuous piecewise linear functions. Another example is the Taylor-Hood elements (with order $k = 2$) in which the velocity is approximated by continuous piecewise quadratics and the pressure by continuous piecewise linear functions [22].

The discrete space for the Darcy pressure is

$$M^h \subset \{q_2 \in H^1(\Omega_2) : \quad q_2 = 0 \text{ on } \Gamma_{2\mathrm{D}}\},$$

that contains continuous piecewise polynomials of degree k. We define the following bilinear forms for the CG-CG scheme:

$$
\begin{aligned}
\forall \boldsymbol{v}, \boldsymbol{w} \in \boldsymbol{X}^h, \quad & a_{\mathrm{NS}}(\boldsymbol{v}, \boldsymbol{w}) = 2\nu(\boldsymbol{D}(\boldsymbol{v}), \boldsymbol{D}(\boldsymbol{w}))_{\Omega_1}, \\
\forall \boldsymbol{v} \in \boldsymbol{X}^h, \forall q_1 \in Q^h, \quad & b_{\mathrm{NS}}(\boldsymbol{v}, q_1) = -(q_1, \nabla\cdot\boldsymbol{v})_{\Omega_1}, \\
\forall \boldsymbol{z}, \boldsymbol{v}, \boldsymbol{w} \in \boldsymbol{X}^h, \quad & c_{\mathrm{NS}}(\boldsymbol{z}, \boldsymbol{v}, \boldsymbol{w}) = \frac{1}{2}(\boldsymbol{z}\cdot\nabla\boldsymbol{v}, \boldsymbol{w})_{\Omega_1} - \frac{1}{2}(\boldsymbol{z}\cdot\nabla\boldsymbol{w}, \boldsymbol{v})_{\Omega_1} + \frac{1}{2}(\boldsymbol{z}\cdot\boldsymbol{n}_{12}, \boldsymbol{v}\cdot\boldsymbol{w})_{\Gamma_{12}}, \\
\forall q_2, t_2 \in M^h, \quad & a_{\mathrm{D}}(q_2, t_2) = \Big(\boldsymbol{K}\nabla q_2, \nabla t_2\Big)_{\Omega_2}, \\
\forall \boldsymbol{v} \in \boldsymbol{X}^h, \forall q_2 \in M^h, \; & L(\boldsymbol{v}, q_2) = (\boldsymbol{f}_1, \boldsymbol{v})_{\Omega_1} + (\boldsymbol{f}_2, q_2)_{\Omega_2} + (g_{\mathrm{N}}, q_2)_{\Gamma_{2\mathrm{N}}}.
\end{aligned}
$$

With these definitions and with the small data condition, we can prove existence and uniqueness of the finite element solution of (11)-(12). In addition, there is a constant C independent of the mesh size h such that the following optimal a priori error estimates hold.

$$
\|\boldsymbol{D}(\boldsymbol{u}-\boldsymbol{U}^h)\|_{L^2(\Omega_1)} + \|p_1 - P_1^h\|_{L^2(\Omega_1)} + \|\boldsymbol{K}^{1/2}\nabla(p_2 - P_2^h)\|_{L^2(\Omega_2)} \le Ch^k.
$$

The proof of these results follows very closely the proof given in [13].

Remark: The case of nonhomogeneous Dirichlet boundary conditions on the boundary $\Gamma_{2\mathrm{D}}$ is handled by the usual technique of lifting the boundary condition [23]. The error analysis is very similar to the case of homogeneous Dirichlet boundary conditions.

2.2 Discontinuous Galerkin finite element scheme (DG-DG)

The mesh $\mathcal{E}^h$ is allowed to be nonconforming in the interior of each free flow region or each porous medium. We write $\mathcal{E}^h = \mathcal{E}_1^h \cup \mathcal{E}_2^h$ where $\mathcal{E}_i^h$ is the mesh restricted to Ω_i. We denote one generic mesh element by E and one generic edge by e. The unknowns are approximated by discontinuous piecewise polynomials. The finite-dimensional spaces are defined for any positive integers k_1 and k_2:

$$
\begin{aligned}
\boldsymbol{X}^h &= \{\boldsymbol{v} \in (L^2(\Omega_1))^2 : \boldsymbol{v}|_E \in \mathbb{P}_{k_1}(E)\}, \\
Q^h &= \{q_1 \in L^2(\Omega_1) : q_1|_E \in \mathbb{P}_{k_1-1}(E)\}, \\
M^h &= \{q_2 \in L^2(\Omega_2) : q_2|_E \in \mathbb{P}_{k_2}(E)\}.
\end{aligned}
$$

Before defining the bilinear forms, we introduce further notation that is standard to the DG method. Let Γ_1^h (resp. Γ_2^h) denote the set of interior edges to Ω_1 (resp. Ω_2) and boundary edges that belong to Γ_1 (resp. $\Gamma_{2\mathrm{D}}$). In other words, $\Gamma_1^h \cup \Gamma_2^h$ contains all edges except those that form the interface Γ_{12} and the Neumann boundary $\Gamma_{2\mathrm{N}}$. For each edge e in $\Gamma_1^h \cup \Gamma_2^h$ we fix a unit normal vector denoted $\boldsymbol{n}_e$. If the edge e is a boundary edge, the vector $\boldsymbol{n}_e$ coincides with the unit normal vector exterior to Ω. For any two triangles E_i and E_j (with $i < j$) that share a common edge e, the vector $\boldsymbol{n}_e$ points from E_i to E_j. The jump function $[v]$ and average function $\{v\}$ of a discontinuous piecewise polynomial v are given by:

$$\{v\} = \frac{1}{2}(v|_{E_i}) + \frac{1}{2}(v|_{E_j}), \quad [v] = (v|_{E_i}) - (v|_{E_j}).$$

We abuse the notation and denote the trace of v on a boundary edge by $v = [v] = \{v\}$. The bilinear forms are defined as follows:

$$\begin{aligned}
\forall \boldsymbol{v}, \boldsymbol{w} \in \boldsymbol{X}^h, \quad & a_{\mathrm{NS}}(\boldsymbol{v}, \boldsymbol{w}) = 2\nu \sum_{E \in \mathcal{E}_1^h} (\boldsymbol{D}(\boldsymbol{v}), \boldsymbol{D}(\boldsymbol{w}))_E + \nu \sum_{e \in \Gamma_1^h} \frac{\sigma_e}{|e|}([\boldsymbol{v}], [\boldsymbol{w}])_e \\
& -2\nu \sum_{e \in \Gamma_1^h} (\{\boldsymbol{D}(\boldsymbol{v})\boldsymbol{n}_e\}, [\boldsymbol{w}])_e + 2\nu\epsilon_1 \sum_{e \in \Gamma_1^h} (\{\boldsymbol{D}(\boldsymbol{w})\boldsymbol{n}_e\}, [\boldsymbol{v}])_e, \\
\forall \boldsymbol{v} \in \boldsymbol{X}^h, \forall q_1 \in Q^h, \quad & b_{\mathrm{NS}}(\boldsymbol{v}, q_1) = -\sum_{E \in \mathcal{E}_1^h} (q_1, \nabla \cdot \boldsymbol{v})_E + \sum_{e \in \Gamma_1^h} (\{q_1\}, [\boldsymbol{v}] \cdot \boldsymbol{n}_e)_e, \\
\forall q_2, t_2 \in M^h, \quad & a_{\mathrm{D}}(q_2, t_2) = \sum_{E \in \mathcal{E}_2^h} (\boldsymbol{K}\nabla q_2, \nabla t_2)_E + \sum_{e \in \Gamma_h^2} \frac{\sigma_e}{|e|}([q_2], [t_2])_e \\
& - \sum_{e \in \Gamma_2^h} (\{\boldsymbol{K}\nabla q_2 \cdot \boldsymbol{n}_e\}[t_2])_e + \epsilon_2 \sum_{e \in \Gamma_2^h} (\{\boldsymbol{K}\nabla t_2 \cdot \boldsymbol{n}_e\}, [q_2])_e, \\
\forall \boldsymbol{v} \in \boldsymbol{X}^h, \forall q_2 \in M^h, \quad & L(\boldsymbol{v}, q_2) = (\boldsymbol{f}_1, \boldsymbol{v})_{\Omega_1} + (f_2, q_2)_{\Omega_2} + (g_{\mathrm{N}}, q_2)_{\Gamma_{2\mathrm{N}}}.
\end{aligned}$$

The length of one edge e is denoted by $|e|$. The parameter $\sigma_e \geq 0$ is the penalty parameter. The coefficients $\epsilon_1, \epsilon_2 \in \{-1, +1\}$ are the symmetrization parameters. We assume that σ_e is large enough if ϵ_1 or ϵ_2 takes the value -1. The DG discretization of the nonlinear operator $\boldsymbol{u} \cdot \nabla \boldsymbol{u}$ is based on an upwinding technique [24] and its definition requires additional notation.
For an element $E \in \mathcal{E}_1^h$, we denote by $\boldsymbol{n}_E$ the outward normal to E, and we denote by $\boldsymbol{v}^{\mathrm{int}}$ (resp. $\boldsymbol{v}^{\mathrm{ext}}$) the trace of the function $\boldsymbol{v}$ on a side of E coming from the interior of E (resp. the exterior of E). When the side of E belongs to Γ_1, then by convention we set $\boldsymbol{v}^{\mathrm{int}} = \boldsymbol{v}$ and $\boldsymbol{v}^{\mathrm{ext}} = \boldsymbol{0}$. Then we define:

$$\begin{aligned}
\forall \boldsymbol{z}, \boldsymbol{v}, \boldsymbol{w} \in \boldsymbol{X}^h, \quad & c_{\mathrm{NS}}(\boldsymbol{z}; \boldsymbol{v}, \boldsymbol{w}) = \sum_{E \in \mathcal{E}_1^h} (\boldsymbol{z} \cdot \nabla \boldsymbol{v}, \boldsymbol{w})_E + \frac{1}{2} \sum_{E \in \mathcal{E}_1^h} (\nabla \cdot \boldsymbol{z}, \boldsymbol{v} \cdot \boldsymbol{w})_E \\
& -\frac{1}{2} \sum_{e \in \Gamma_1^h} ([\boldsymbol{z}] \cdot \boldsymbol{n}_e, \{\boldsymbol{v} \cdot \boldsymbol{w}\})_e + \sum_{E \in \mathcal{E}_1^h} (|\{\boldsymbol{z}\} \cdot \boldsymbol{n}_E|(\boldsymbol{v}^{\mathrm{int}} - \boldsymbol{v}^{\mathrm{ext}}), \boldsymbol{w}^{\mathrm{int}})_{\partial E_-(\boldsymbol{z}) \setminus \Gamma_{12}},
\end{aligned}$$

where

$$\partial E_-(\boldsymbol{z}) = \{\boldsymbol{x} \in \partial E\,;\, \{\boldsymbol{z}(\boldsymbol{x})\} \cdot \boldsymbol{n}_E < 0\}.$$

The linear form L is the same as in Section 2.1.

With these definitions and with the assumption of small data, we can prove existence and uniqueness of the DG solution of (11)-(12). In addition, there is a constant C independent of the mesh size h (but dependent on the viscosity

ν and penalty parameter σ_e) such that the following optimal a priori error estimates hold.

$$\Big(\sum_{E\in\mathcal{E}_1^h}\|\boldsymbol{D}(\boldsymbol{u}-\boldsymbol{U}^h)\|^2_{L^2(E)}+\sum_{e\in\Gamma_1^h}|e|^{-1}\|[\boldsymbol{U}^h]\|^2_{L^2(e)}\Big)^{1/2}+\|p_1-P_1^h\|_{L^2(\Omega_1)}$$
$$+\Big(\sum_{E\in\mathcal{E}_2^h}\|\boldsymbol{K}^{1/2}\nabla(p_2-P_2^h)\|^2_{L^2(E)}+\sum_{e\in\Gamma_2^h}|e|^{-1}\|[P_2^h]\|^2_{L^2(e)}\Big)^{1/2}\le C(h^{k_1}+h^{k_2}).$$

Remark: If non-homogeneous boundary conditions are prescribed for the pressure on $\Gamma_{2\mathrm{D}}$, they are weakly imposed by adding terms to the form L [14]. This is different from the finite element method in which the Dirichlet boundary conditions are imposed strongly.

2.3 Coupled continuous Galerkin with discontinuous Galerkin finite element scheme (CG-DG)

We propose to use the continuous finite element method in Ω_1 and the discontinuous Galerkin method in Ω_2 for several reasons. First we want to use the best-suited method in each region. It was shown that the continuous finite element method can produce non-physical flow in a fractured porous medium [25]. As DG methods are locally mass conservative, they are appropriate for flow and transport problems in heterogeneous porous media. Second, there exist legacy codes for solving the Navier-Stokes equation with the classical finite element method whereas DG software for these problems is not readily available.

In this multinumerics scheme, we use the forms $a_{\mathrm{NS}}, b_{NS}, c_{\mathrm{NS}}$ defined in Section 2.1 and the form a_{D} defined in Section 2.2. We recall the discrete spaces and forms below. The spaces $\boldsymbol{X}^h\subset\{\boldsymbol{v}\in H^1(\Omega_1)^2:\ \boldsymbol{v}=0\text{ on }\Gamma_1\}$ and $Q^h\subset L^2(\Omega)$ satisfy an inf-sup condition and are of order k_1. The space M^h consists of discontinuous piecewise polynomials of degree k_2. For readability, we recall the bilinear forms for the CG-DG scheme:

$$\forall\boldsymbol{v},\boldsymbol{w}\in\boldsymbol{X}^h,\quad a_{\mathrm{NS}}(\boldsymbol{v},\boldsymbol{w})=2\nu(\boldsymbol{D}(\boldsymbol{v}),\boldsymbol{D}(\boldsymbol{w}))_{\Omega_1},$$
$$\forall\boldsymbol{v}\in\boldsymbol{X}^h,\forall q_1\in Q^h,\quad b_{\mathrm{NS}}(\boldsymbol{v},q_1)=-(q_1,\nabla\cdot\boldsymbol{v})_{\Omega_1},$$
$$\forall\boldsymbol{z},\boldsymbol{v},\boldsymbol{w}\in\boldsymbol{X}^h,\quad c_{\mathrm{NS}}(\boldsymbol{z},\boldsymbol{v},\boldsymbol{w})=\frac{1}{2}(\boldsymbol{z}\cdot\nabla\boldsymbol{v},\boldsymbol{w})_{\Omega_1}-\frac{1}{2}(\boldsymbol{z}\cdot\nabla\boldsymbol{w},\boldsymbol{v})_{\Omega_1}+\frac{1}{2}(\boldsymbol{z}\cdot\boldsymbol{n}_{12},\boldsymbol{v}\cdot\boldsymbol{w})_{\Gamma_{12}},$$
$$\forall q_2,t_2\in M^h,\quad a_{\mathrm{D}}(q_2,t_2)=\sum_{E\in\mathcal{E}_2^h}(\boldsymbol{K}\nabla q_2,\nabla t_2)_E+\sum_{e\in\Gamma_h^2}\frac{\sigma_e}{|e|}([q_2],[t_2])_e$$
$$-\sum_{e\in\Gamma_2^h}(\{\boldsymbol{K}\nabla q_2\cdot\boldsymbol{n}_e\}[t_2])_e+\epsilon_2\sum_{e\in\Gamma_2^h}(\{\boldsymbol{K}\nabla t_2\cdot\boldsymbol{n}_e\},[q_2])_e.$$

The linear form L is the same as in Section 2.1.

With these definitions and under a small data condition, we obtain existence and uniqueness of the numerical solution. In addition the scheme is convergent with optimal order. There is a constant C independent of the mesh size h such that the following a priori error estimates hold.

$$\begin{aligned}
&\|\boldsymbol{D}(\boldsymbol{u}-\boldsymbol{U}^h)\|_{L^2(\Omega_1)} + \|p_1 - P_1^h\|_{L^2(\Omega_1)} \\
+&\Big(\sum_{E\in\mathcal{E}_2^h} \|\boldsymbol{K}^{1/2}\nabla(p_2 - P_2^h)\|^2_{L^2(E)} + \sum_{e\in\Gamma_2^h} |e|^{-1}\|[P_2^h]\|^2_{L^2(e)}\Big)^{1/2} \leq C(h^{k_1} + h^{k_2}).
\end{aligned}$$

3 Numerical Convergence

In this section we investigate the convergence of the methods presented above with respect to the grid parameter h. The computational domain $\Omega \subset \mathbb{R}^2$ is divided into $\Omega_1 = (0,1)\times(1,2)$ and $\Omega_2 = (0,1)\times(0,1)$ with interface $\Gamma_{12} = (0,1)\times\{1\}$. We consider Neumann boundary conditions on $\Gamma_{2\mathrm{N}} = \{0,1\}\times(0,1)$, the lateral boundary of Ω_2 and Dirichlet boundary conditions on the bottom boundary $\Gamma_{2\mathrm{D}} = (0,1)\times\{0\}$. The parameters are $\nu = 1$, $\alpha = 1$ and $\boldsymbol{K} = \mathbf{I}$. The tolerance is $\delta = 10^{-12}$ for the Picard iterations. Throughout the paper, the linear systems are solved using a direct sparse solver.

The boundary conditions are chosen so that the exact solution to the coupled Navier-Stokes/Darcy problem is:

$$\begin{aligned}
\boldsymbol{u}_1(x,y) = \Big(-\cos(\frac{\pi}{2}y)\sin(\frac{\pi}{2}x) + 1.0, \sin(\frac{\pi}{2}y)\cos(\frac{\pi}{2}x) - 1.0 + x\Big), \quad &\text{in } \Omega_1,\\
p_1(x,y) = 1 - x, \quad &\text{in } \Omega_1,\\
p_2(x,y) = \frac{2}{\pi}\cos(\frac{\pi}{2}x)\cos(\frac{\pi}{2}y) - y(x-1), \quad &\text{in } \Omega_2.
\end{aligned}$$

3.1 Continuous Galerkin finite element scheme

The finite element spaces are the MINI finite element for the Navier-Stokes region and continuous piecewise linears for the Darcy region. We compute the L^2 errors for velocity and pressure in both regions, as well as the H^1 error for the Navier-Stokes velocity. The coarse mesh consists of 16 triangles with a mesh size $h = \sqrt{2}/2$ and the finest mesh contains 4096 triangles with a mesh size $h = \sqrt{2}/32$. In Table 1 we observe a convergence rate of order one in the Navier-Stokes and Darcy velocity as expected. The numerical rate is computed with the errors obtained on the two finest meshes. The convergence rate for the Navier-Stokes pressure is better than the expected rate of one. We also observe a rate of two for the L^2 norm of the Navier-Stokes velocity and Darcy pressure, which is consistent with the usual approximation results [23].

$\sqrt{2}/h$	$\|\|\boldsymbol{U}^h - \boldsymbol{u}\|\|_{L^2(\Omega_1)}$	$\|\|P_1^h - p_1\|\|_{L^2(\Omega_1)}$	$\|\|\boldsymbol{D}(\boldsymbol{U}^h - \boldsymbol{u})\|\|_{L^2(\Omega_1)}$	$\|\|P_2^h - p_2\|\|_{L^2(\Omega_2)}$	$\|\|\nabla(P_2^h - p_2)\|\|_{L^2(\Omega_2)}$
2	7.173×10^{-2}	4.143×10^{0}	7.351×10^{-1}	4.080×10^{-2}	2.330×10^{-1}
4	1.812×10^{-2}	5.429×10^{-1}	2.433×10^{-1}	1.270×10^{-2}	1.405×10^{-1}
8	4.445×10^{-3}	1.598×10^{-1}	1.135×10^{-1}	3.417×10^{-3}	7.286×10^{-2}
16	1.097×10^{-3}	5.320×10^{-2}	5.540×10^{-2}	8.959×10^{-4}	3.670×10^{-2}
32	2.730×10^{-4}	1.885×10^{-2}	2.735×10^{-2}	1.962×10^{-4}	1.838×10^{-2}
rate	2.00	1.58	1.00	2.00	1.00

Table 1
Numerical errors and convergence rates for CG-CG scheme of order one.

3.2 Discontinuous Galerkin finite element scheme

We first approximate the Navier-Stokes velocity and the Darcy pressure by discontinuous piecewise quadratics. We always use a polynomial degree for the Navier-Stokes pressure that is one order less than the degree for Navier-Stokes velocity. In this case, we use discontinuous piecewise linears for the Navier-Stokes pressure. The other parameters in the DG scheme are chosen as: $\epsilon_1 = \epsilon_2 = 1$ and $\sigma_e = 1$. Table 2 shows the errors and the corresponding convergence rates, obtained on a sequence of meshes as in the above section. We obtain a convergence rate of order 2 as predicted by the theory. Similar results are obtained if $\epsilon_1 = \epsilon_2 = -1$ with $\sigma_e = 10$. We now increase the polynomial degree

$\sqrt{2}/h$	$\|\|\boldsymbol{U}^h - \boldsymbol{u}\|\|_{L^2(\Omega_1)}$	$\|\|P_1^h - p_1\|\|_{L^2(\Omega_1)}$	$\|\|\boldsymbol{D}(\boldsymbol{U}^h - \boldsymbol{u})\|\|_{L^2(\Omega_1)}$	$\|\|P_2^h - p_2\|\|_{L^2(\Omega_2)}$	$\|\|\nabla(P_2^h - p_2)\|\|_{L^2(\Omega_2)}$
2	4.682×10^{-3}	7.554×10^{-2}	7.954×10^{-2}	5.504×10^{-3}	3.470×10^{-2}
4	6.309×10^{-4}	1.828×10^{-2}	1.255×10^{-2}	1.365×10^{-3}	8.824×10^{-3}
8	9.145×10^{-5}	4.477×10^{-3}	3.082×10^{-3}	3.447×10^{-4}	2.215×10^{-3}
16	1.598×10^{-5}	1.104×10^{-3}	7.602×10^{-4}	8.679×10^{-5}	6.281×10^{-4}
32	3.398×10^{-6}	2.739×10^{-4}	1.887×10^{-4}	2.178×10^{-5}	1.569×10^{-4}
rate	2.23	2.01	2.01	1.99	2.00

Table 2
Numerical errors and convergence rates for the DG-DG scheme of order two.

by one in each region. The lack of continuity requirement with the DG method allows for a very easy implementation of high order approximation. Table 3 shows the errors and rates for the case of piecewise cubic approximations of Navier-Stokes velocity and Darcy pressure. Similarly Table 4 presents the results in the case of discontinuous piecewise quartic approximations of the Navier-Stokes velocity and Darcy pressure. The advantage of using high order is clear for this test problem. The high order solution is more accurate on a coarser mesh than the low order solution on a finer mesh. For instance, the L^2 error in the piecewise quartic Navier-Stokes velocity obtained on the mesh of size $h = \sqrt{2}/8$ is 10^2 smaller than the error in the piecewise quadratic

$\sqrt{2}/h$	$\|\|\boldsymbol{U}^h - \boldsymbol{u}\|\|_{L^2(\Omega_1)}$	$\|\|P_1^h - p_1\|\|_{L^2(\Omega_1)}$	$\|\|\boldsymbol{D}(\boldsymbol{U}^h - \boldsymbol{u})\|\|_{L^2(\Omega_1)}$	$\|\|P_2^h - p_2\|\|_{L^2(\Omega_2)}$	$\|\|\nabla(P_2^h - p_2)\|\|_{L^2(\Omega_2)}$
2	4.260×10^{-4}	1.058×10^{-2}	9.766×10^{-3}	2.549×10^{-4}	4.095×10^{-3}
4	2.185×10^{-5}	9.518×10^{-4}	9.707×10^{-4}	1.724×10^{-5}	4.258×10^{-4}
8	1.425×10^{-6}	1.169×10^{-4}	1.219×10^{-4}	1.153×10^{-6}	5.521×10^{-5}
16	9.195×10^{-8}	1.465×10^{-5}	1.518×10^{-5}	7.411×10^{-8}	7.003×10^{-6}
rate	3.95	2.99	3.00	3.96	2.98

Table 3
Numerical errors and convergence rates for the DG-DG scheme of order three.

velocity on the mesh of size $h = \sqrt{2}/32$. The former problem (i.e. for quartic approximations) requires 7040 degrees of freedom whereas the latter problem (i.e. for quadratic approximations) requires 43008 degrees of freedom.

$\sqrt{2}/h$	$\|\|\boldsymbol{U}^h - \boldsymbol{u}\|\|_{L^2(\Omega_1)}$	$\|\|P_1^h - p_1\|\|_{L^2(\Omega_1)}$	$\|\|\boldsymbol{D}(\boldsymbol{U}^h - \boldsymbol{u})\|\|_{L^2(\Omega_1)}$	$\|\|P_2^h - p_2\|\|_{L^2(\Omega_2)}$	$\|\|\nabla(P_2^h - p_2)\|\|_{L^2(\Omega_2)}$
2	3.335×10^{-5}	1.041×10^{-3}	9.075×10^{-4}	2.168×10^{-5}	3.792×10^{-4}
4	1.154×10^{-6}	6.229×10^{-5}	6.570×10^{-5}	1.767×10^{-6}	2.813×10^{-5}
8	3.565×10^{-8}	3.516×10^{-6}	4.068×10^{-6}	1.096×10^{-7}	1.753×10^{-6}
rate	5.02	4.15	4.01	4.01	4.00

Table 4
Numerical errors and convergence rates for the DG-DG scheme of order four.

3.3 Coupled continuous Galerkin with discontinuous Galerkin finite element scheme

In this multinumerics scheme, Navier-Stokes flow is approximated by the MINI finite element whereas Darcy flow is approximated by discontinuous piecewise polynomials. The coefficients in the DG method are chosen as: $\epsilon_1 = \epsilon_2 = 1$ and $\sigma_e = 1$. Table 5 shows the numerical errors and convergence rates if the DG method of order 1 is used for the Darcy region. The resulting rate is of order one as predicted by the theory. Next we increase the polynomial degree in the Darcy region to two and repeat the simulations. The results are presented in Table 6. It is clear that the order two approximation achieves higher accuracy on coarser meshes compared to the order 1 approximation. We also observe a higher convergence rate of two for the Darcy pressure in Ω_2. However since we are still using a lower order approximation in Ω_1 there is no improvement in the quality of the solution in Ω_1.

From these experiments, we have confirmed the optimal numerical convergence of all three methods. We note that the discontinuous Galerkin method seems better suited for higher order approximations due to the ease of implementation.

$1/h$	$\|\|\boldsymbol{U}^h - \boldsymbol{u}\|\|_{L^2(\Omega_1)}$	$\|\|P_1^h - p_1\|\|_{L^2(\Omega_1)}$	$\|\|\boldsymbol{D}(\boldsymbol{U}^h - \boldsymbol{u})\|\|_{L^2(\Omega_1)}$	$P_2^h - p_2$	$\|\|\nabla(P_2^h - p_2)\|\|_{L^2(\Omega_2)}$
2	6.058×10^{-2}	2.809×10^{0}	6.566×10^{-1}	3.479×10^{-2}	2.025×10^{-1}
4	1.615×10^{-2}	3.999×10^{-1}	2.337×10^{-1}	9.361×10^{-3}	1.026×10^{-2}
8	3.769×10^{-3}	1.201×10^{-1}	1.128×10^{-1}	2.326×10^{-3}	4.948×10^{-2}
16	9.350×10^{-4}	4.188×10^{-2}	5.557×10^{-2}	5.719×10^{-4}	2.427×10^{-2}
32	2.335×10^{-4}	1.482×10^{-2}	2.751×10^{-2}	1.412×10^{-4}	1.201×10^{-2}
rate	2.00	1.50	1.00	2.00	1.00

Table 5
Numerical errors and convergence rates for CG-DG scheme of order one.

$1/h$	$\|\|\boldsymbol{U}^h - \boldsymbol{u}\|\|_{L^2(\Omega_1)}$	$\|\|P_1^h - p_1\|\|_{L^2(\Omega_1)}$	$\|\|\boldsymbol{D}(\boldsymbol{U}^h - \boldsymbol{u})\|\|_{L^2(\Omega_1)}$	$\|\|P_2^h - p_2\|\|_{L^2(\Omega_2)}$	$\|\|\nabla(P_2^h - p_2)\|\|_{L^2(\Omega_2)}$
2	6.058×10^{-2}	2.817×10^{0}	6.566×10^{-1}	4.841×10^{-3}	4.254×10^{-2}
4	1.615×10^{-2}	4.015×10^{-1}	2.337×10^{-1}	1.106×10^{-3}	1.154×10^{-2}
8	3.770×10^{-3}	1.203×10^{-1}	1.129×10^{-1}	3.041×10^{-4}	2.875×10^{-3}
16	9.352×10^{-4}	4.189×10^{-2}	5.557×10^{-2}	7.613×10^{-5}	7.155×10^{-4}
32	2.334×10^{-4}	1.482×10^{-2}	2.751×10^{-2}	1.915×10^{-5}	1.789×10^{-4}
rate	2.00	1.50	1.00	2.00	2.00

Table 6
Numerical errors and convergence rates for CG-DG scheme of order two.

4 Numerical Examples

In this section, we study the robustness of all three schemes with respect to the characteristics of the porous medium, the interface and the fluid. Unless specified otherwise, the kinematic viscosity ν is equal to 1.0 and the parameter α in the Beavers-Joseph-Saffman's law is equal to 0.1 as reported in [18]. In this section, the CG-CG scheme uses the MINI elements in Ω_1 and continuous piecewise linears in Ω_2. Similarly, the CG-DG scheme employs the MINI elements in Ω_1 and discontinuous polynomials of degree one or two in Ω_2. Finally the DG-DG scheme uses discontinuous polynomials of degree one or two in the whole domain. The DG parameters for the solutions shown are $\epsilon_1 = 1, \epsilon_2 = 1, \sigma_e = 1$ but we discuss the case of symmetric DG formulations as well.

4.1 Polygonal interface

The domain is $\Omega = (0,2) \times (0,1.25)$ divided into two regions by a polygonal line Γ_{12} that consists of three forward steps of height equal to 1/4. The porous medium has intrinsic permeability $10^{-5}\mathbf{I}$ and it is the subregion below the interface (see Fig. 1). The Navier-Stokes velocity on Γ_1 is equal to $(-3(y-5/4)(y-1/2), 0)$ and zero Neumann boundary conditions are imposed for the Darcy pressure on the vertical sides $\{0\} \times (0,0.5)$ and $\{2\} \times (0,1.25)$. Zero Dirichlet boundary condition is imposed on the Darcy pressure on the bottom side of Ω. We also have: $\boldsymbol{f}_1 = \mathbf{0}, f_2 = 0$. The coarse mesh contains 2469

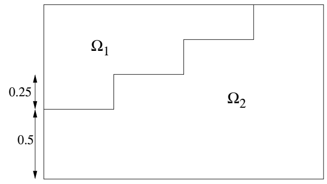

Fig. 1. Computational domain with polygonal interface.

elements in the Navier-Stokes region and 3291 elements in the Darcy region. The number of degrees of freedom are 18714 for the CG-DG solution, 27156 for the DG-DG solution of order one and 56781 for the DG-DG solution of order two. For these three choices, convergence is obtained with 4 Picard iterations for a tolerance $\delta = 10^{-6}$. Fig. 2 (a)-(c) shows the pressure approximations

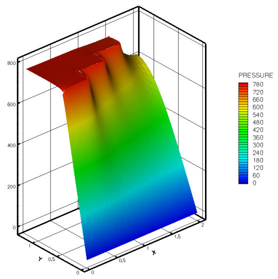

(a) CG-DG pressure of order one

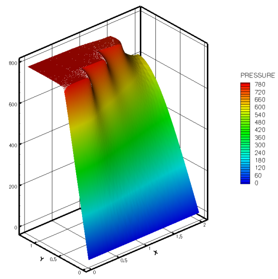

(b) DG-DG pressure of order one

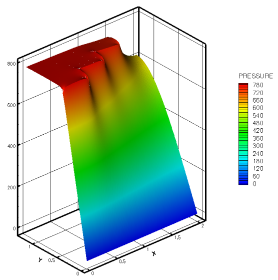

(c) DG-DG pressure of order two

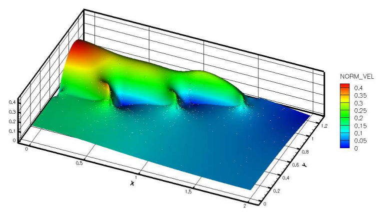

(d) DG-DG velocity of order two

Fig. 2. Pressure contours (a)-(c) and norm of velocity contours (d).

and Fig. 2 (d) shows the norm of velocity contours. To better compare the solutions, we extract the solutions at one hundred points uniformly distributed on the lines $y = 0.6$, $y = 0.8$ and $y = 0.9$. The profiles for the pressure are shown in Fig. 3. Each figure shows the curves obtained by the CG-CG method, the CG-DG method for $(k_1, k_2) = (1, 1)$ and $(k_1, k_2) = (1, 2)$, and the DG-DG method for $k_1 = k_2 = 1$ and $k_1 = k_2 = 2$. We plot each solution obtained on the coarse mesh, and also on a fine mesh that contains 23040 elements. This yields a total of ten curves. The DG-DG profiles are dotted lines and the other profiles are solid lines. From Fig. 3 we observe that all solutions for the pressure are similar. There is a pressure drop corresponding to the location of the interface along each line. The largest pressure in the Navier-Stokes region is obtained with the DG-DG method. We also extract the norm of the velocity

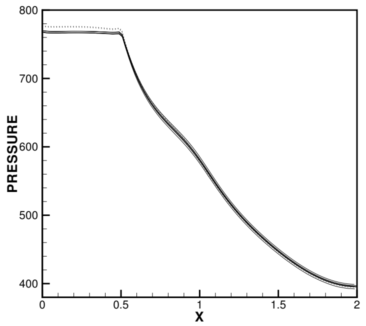

(a) Along line $y = 0.6$

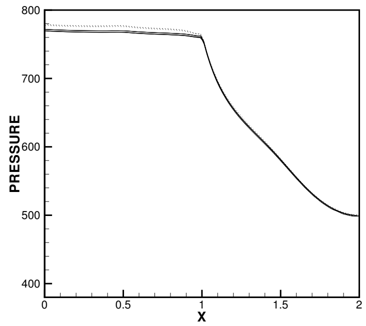

(b) Along line $y = 0.8$

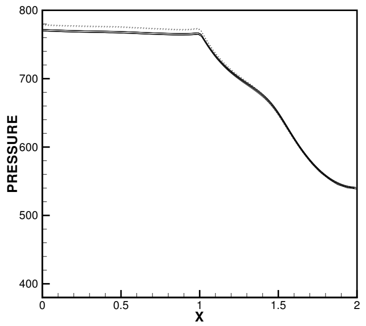

(c) Along line $y = 0.9$

Fig. 3. Pressure profiles along horizontal lines for all methods on coarse and fine meshes.

along the same horizontal lines. The profiles are shown on Fig. 4. Along the line $y = 0.9$ all profiles coincide. Along the line $y = 0.8$ the CG-CG and CG-DG methods yield similar profiles, whereas the DG-DG velocity is smaller in the free flow region that is above the first step. Finally along the line $y = 0.6$ the profiles are similar, but the DG-DG norm of velocity is larger before the interface. From these profiles, we conclude that the overall flow field is the same for all methods. However there are subregions of the free flow for which the DG-DG velocity differs. This is due to the larger pressure profile for the DG-DG solution in the Navier-Stokes region.

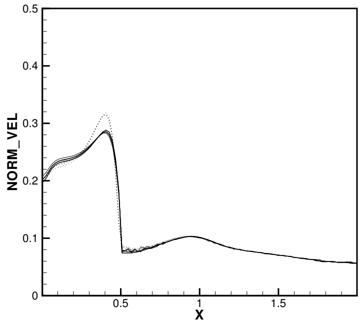

(a) Along line $y = 0.6$

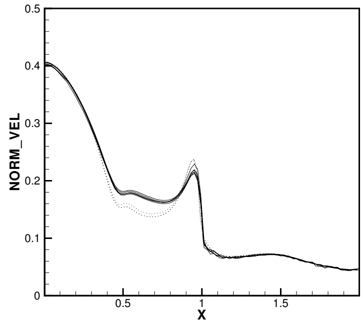

(b) Along line $y = 0.8$

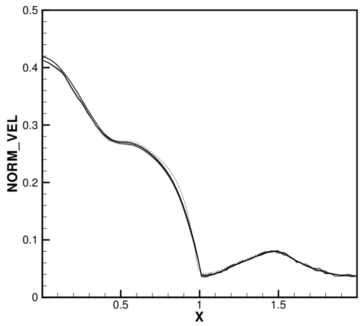

(c) Along line $y = 0.9$

Fig. 4. Norm of velocity profiles along horizontal lines for all methods on coarse and fine meshes.

4.2 Discontinuous permeability field

4.2.1 Rock in porous medium

The free flow domain is $\Omega_1 = (0, 1) \times (1, 2)$ and the porous medium is $\Omega_2 = (0, 1) \times (0, 1)$. The porous medium has a circular region centered at $(x, y) = (0.5, 0.5)$ with intrinsic permeability equal to $10^{-12}\mathbf{I}$ surrounded by a matrix with intrinsic permeability equal to $\mathbf{I}$. We impose a Dirichlet boundary condition $\boldsymbol{u}_1 = (0, -1)$ on $\Gamma_1 = \partial\Omega_1 \backslash \Gamma_{12}$ and zero Dirichlet and Neumann conditions on the bottom and lateral boundaries of the domain Ω_2 respectively. The body forces are $\boldsymbol{f}_1 = (0, 1)$ and $f_2 = 0$.

Fig. 5(a)-(c) show the streamlines and the contours of Euclidean norm of velocity for the solutions obtained from each scheme on a mesh with 826 triangular elements in the porous medium and 206 elements in the free flow region. The CG-CG method yields a system with 1143 degrees of freedom whereas the CG-DG and DG-DG schemes require 3199 and 8046 degrees of freedom respectively. It is clear that we observe the same expected flow pattern from all three schemes and that the CG-CG scheme is the least expensive method for

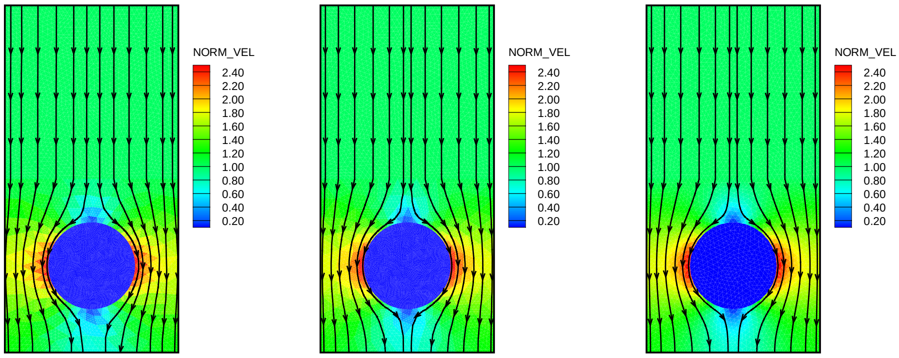

(a) CG-CG solution (b) CG-DG solution (c) DG-DG solution

Fig. 5. Contours of Euclidean norm of velocity and streamlines for case of circular inclusion in porous medium.

this problem. The CG-CG and CG-DG solutions take 5 Picard iterations to converge with a tolerence set at 10^{-12}. The DG-DG scheme converges with 8 Picard iterations.

4.2.2 Vertical faults

In this example, the domain $\Omega = (0,1) \times (0,1.5)$ has two vertical faults (of width equal to 0.05) that allow the fluid to penetrate the porous medium. Fig. 6 shows the location of the faults. The intrinsic permeability for the rock matrix is $10^{-7}\mathbf{I}$. The purpose of this example is to compare the numerical flow obtained if Darcy equations are used inside the faults with the numerical flow obtained if the Navier-Stokes equations are used inside the faults. The parameters for this problem are $\boldsymbol{f}_1 = \mathbf{0}, f_2 = 0, \delta = 10^{-6}$. The velocity on Γ_1 is set equal to $(0, -1/3)$, which means the flow is downward. Zero Neumann and Dirichlet boundary conditions for the Darcy pressure are prescribed on the vertical and horizontal sides of Γ_2 respectively. We first solve the problem

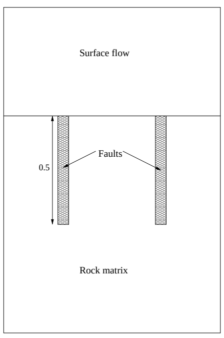

Fig. 6. Computational domain with vertical faults.

by considering the faults belong to the porous medium, i.e. $\Omega_2 = (0,1)^2$. The interface is a simple horizontal line $\Gamma_{12} = (0,1) \times \{1\}$. The intrinsic permeability in the faults is $10^{-1}\mathbf{I}$. In solutions obtained for all three methods of order one are shown in Fig. 7. The same mesh is used for all the simulations. Each figure shows both pressure and norm of velocity: the z-axis corresponds to the discrete pressure and the colors correspond to the distribution of the norm of velocity. We observe that the velocity is larger inside the vertical faults, as expected. Second we modify the problem only by replacing the Darcy equations

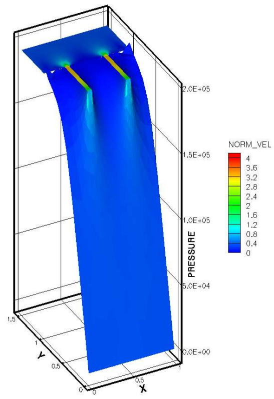

(a) CG-CG (5099 dofs)

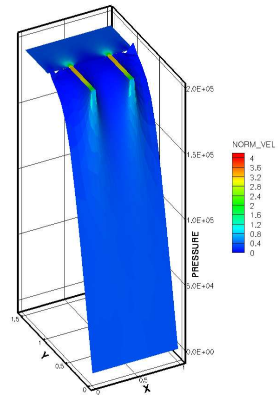

(b) CG-DG (20029 dofs)

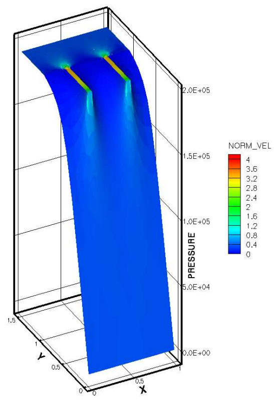

(c) DG-DG (21920 dofs)

Fig. 7. Pressure and velocity with all three methods of order one and with using Darcy equations inside the faults.

by the Navier-Stokes equations inside the vertical faults. We remark that we could also have used an intermediate model by using the Stokes equations inside the faults. In this case, the interface Γ_{12} is a polygonal line and the surface region Ω_1 consists of the two vertical faults plus the region $(0,1) \times (1, 1.5)$.

Fig. 8 shows the solutions of order one obtained with all three methods. As above we observe that the magnitude of the velocity is larger inside the faults. To better compare the different solutions, we extract the norm of the velocity

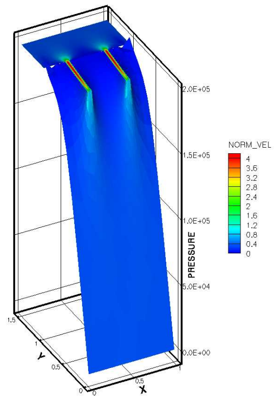

(a) CG-CG (8571 dofs)

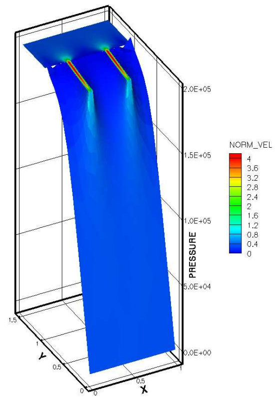

(b) CG-DG (20841 dofs)

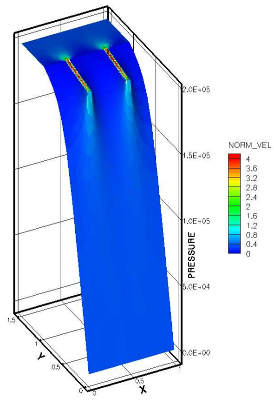

(c) DG-DG (26000 dofs)

Fig. 8. Pressure and velocity with all three methods of order one and with using Navier-Stokes equations inside the faults.

along three horizontal lines at $y = 0.3$, $y = 0.6$ and $y = 0.9$. We also include the DG-DG solution of order two. Fig. 9(a) shows that the output flow is the same independent of all methods and models. Fig. 9(b) shows two interesting points. First inside the faults, the norm of velocity profile is a sharp parabola with a larger magnitude if the Navier-Stokes equations are used. If the Darcy equations are used, the profile is a flat curve with smaller magnitude inside the faults. This difference in velocity can be explained by the fact that flow will be faster in an open fault than in a porous medium with high permeability. Second we see that increasing the polynomial degree for the DG-DG method

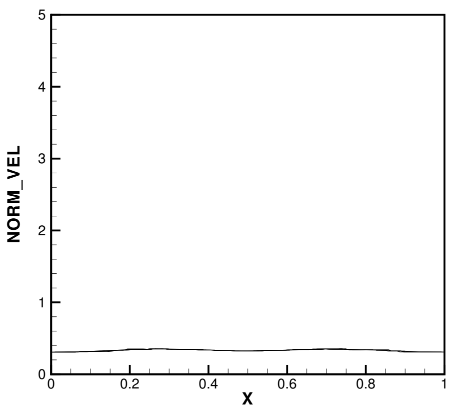

(a) Along line $y = 0.3$

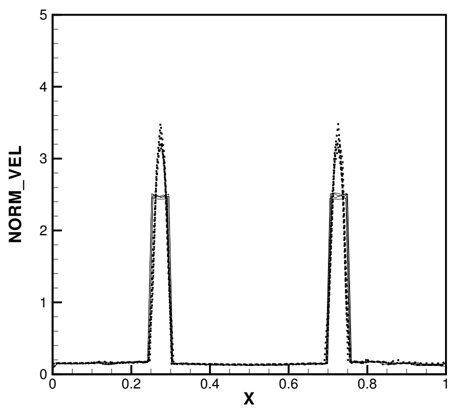

(b) Along line $y = 0.6$

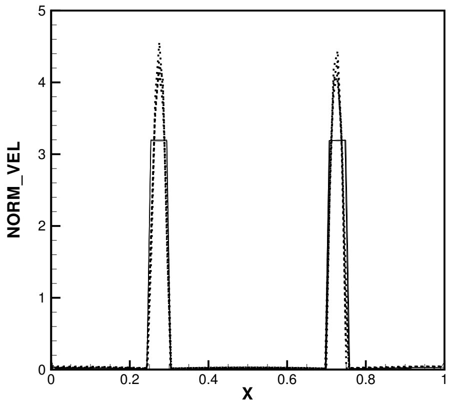

(c) Along line $y = 0.9$

Fig. 9. Profile of norm of velocity for all methods of order one and also for DG-DG of order two. Dotted lines correspond to solutions when the Navier-Stokes equations are used inside the faults.

from 1 to 2 produces a larger magnitude of the velocity in the middle of the faults. Similar observations are made from Fig. 9(c). The difference is that the magnitude of velocity is much larger inside the faults and that the velocity is almost zero outside the faults. In the results above, the DG-DG solutions converge in 5 Picard iterations, the CG-DG solutions in 4 Picard iterations, and the CG-CG in 6 Picard iterations, independently of the choice of the equations used in the faults. We also solved the problem by using the symmetric DG formulation ($\epsilon_1 = \epsilon_2 = -1$). The choice of the penalty is critical in this case. The value $\sigma_e = 10$ (which is usually what is chosen in the literature) does not yield a stable solution. From the paper [26], a lower bound for the penalty value depends on the maximum and minimum permeability values. For this problem, the lower bound is of the order 10^8, which is not a practical choice. This numerical example shows that the use of the Navier-Stokes equations inside the faults is needed if one is interested in the fluctuations of the velocity inside the faults. If the quantity of interest is the output velocity once the flow has passed through the faults, then a Darcy model is sufficient.

4.2.3 Two intersecting slanted fractures

We now test the robustness of the CG-DG method for a problem in which the porous medium contains two slanted fractures that intersect (see [25]). The domain is $\Omega = (0, 1.6) \times (0, 2)$ with $\Omega_2 = (0, 1.6) \times (0, 1.5)$. The rock matrix has intrinsic permeability equal to $10^{-8}\mathbf{I}$ and the two intersecting fractures have intrinsic permeability equal to $10^{-5}\mathbf{I}$. The boundary conditions imposed on the domain are the same as in Section 4.2.1. Fig. 10 shows the location

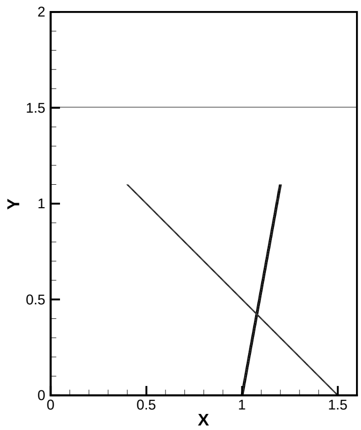

(a) Computational domain

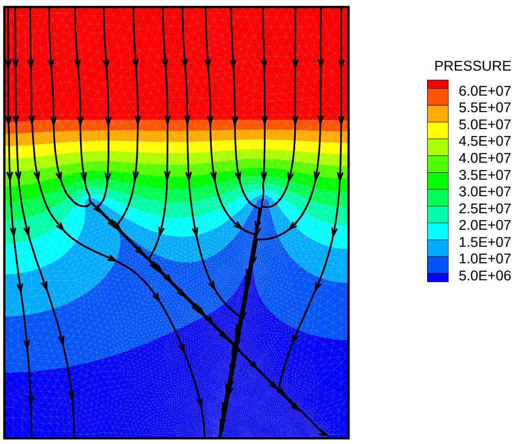

(b) CG-DG pressure and streamlines

Fig. 10. Intersecting fractures in porous medium.

of the fractures and the CG-DG solution with $k_1 = 1$ and $k_2 = 2$. We remark that the left fracture has a smaller width than the right one. The mesh contains 58 elements in the Navier-Stokes region, and 1054 elements in the Darcy subdomain. The mesh elements are finer in a neighborhood containing the fractures. The CG-DG solution converges with 4 Picard iterations, for a problem size equal to 6535. The numerical challenge in this problem is to capture the right flow pattern in the faults in particular in the region of their intersection. We show a zoom of the streamlines in Fig. 11. We clearly see that fluid flows downward either in the left or right fault. Similar results are obtained with the other methods.

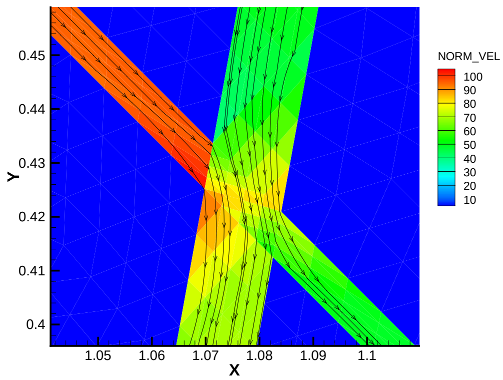

Fig. 11. Zoom on streamlines in the region of intersection of the faults.

4.3 Kinematic viscosity

We consider the effect of the kinematic viscosity ν on the CG-DG coupling of the Navier-Stokes/Darcy coupling. The domain is the same as in Section 3. The boundary conditions are chosen in such a way that the exact solution is:

$$\boldsymbol{u}_1(x,y) = \Big(y^2 - 2y + 1 + \nu(2x-1), x^2 - x - (y-1)2\nu\Big)$$
$$p_1(x,y) = 2\nu(x+y-1.0) + \frac{1}{3} - 4\nu^2$$
$$p_2(x,y) = \Big(x(1-x)(y-1) + \frac{y^3}{3} - y^2 + y\Big) + 2\nu x.$$

The following parameters are fixed: $\alpha = 1$ and $\boldsymbol{K} = \mathbf{I}$. We decrease ν from 1 to 0.001 and for each value of ν, we compute the errors on successive refinements on a coarse mesh with $h = \sqrt{2}/4$ described in Section 3.

Table 7 shows the convergence rates for each variable for different values of ν and error on a fine mesh consisting of 8192 elements using the CG-DG method of order one. We also report N, the number of Picard iterations required for convergence with a tolerance $\delta = 10^{-10}$. We observe optimal convergence rates

ν	N	$\|\|\boldsymbol{U}^h - \boldsymbol{u}\|\|_{L^2(\Omega_1)}$	$\|\|P_1^h - p_1\|\|_{L^2(\Omega_1)}$	$\|\|\boldsymbol{D}(\boldsymbol{U}^h - \boldsymbol{u})\|\|_{L^2(\Omega_1)}$	$\|\|P_2^h - p_2\|\|_{L^2(\Omega_2)}$	$\|\|\nabla(P_2^h - p_2)\|\|_{L^2(\Omega_2)}$
1	8	6.183×10^{-5}(2.00)	7.208×10^{-4} (1.54)	8.485×10^{-3}(1.00)	6.616×10^{-5}(2.00)	7.100×10^{-3}(1.00)
0.1	10	6.201×10^{-5}(2.00)	8.358×10^{-5}(1.68)	8.485×10^{-3}(1.00)	6.615×10^{-5}(2.00)	7.100×10^{-3}(1.00)
0.01	18	6.329×10^{-5}(2.00)	4.089×10^{-5}(1.97)	8.489×10^{-3}(1.00)	6.612×10^{-5}(2.00)	7.100×10^{-3}(1.00)
0.001	23	6.462×10^{-5}(2.00)	4.074×10^{-5}(1.98)	8.897×10^{-3}(1.00)	6.611×10^{-5}(2.00)	7.101×10^{-3}(1.00)

Table 7
Picard iterations, numerical errors and convergence rates of approximations by CG-DG of order one.

for Reynolds number up to 1000 and an increase in the number of Picard iterations required to achieve convergence under the set tolerance.

5 Mass Conservation

5.1 Balance of mass

Mass conservation for the coupled problem (1)-(10) is obtained globally on Ω and can be written as:

$$\int_{\Gamma_1} \boldsymbol{u}_1 \cdot \boldsymbol{n} + \int_{\Gamma_2} \boldsymbol{u}_2 \cdot \boldsymbol{n} - \int_{\Omega_2} f_2 = 0.$$

We recall that $\Gamma_2 = \Gamma_{2\mathrm{N}} \cup \Gamma_{2\mathrm{D}}$. We seek to quantify the mass balance for the three algorithms CG-CG, CG-DG and DG-DG. For the numerical solution, we define the mass balance as:

$$\theta = \int_{\Gamma_1} \boldsymbol{U}^h \cdot \boldsymbol{n} - \int_{\Gamma_2} \boldsymbol{K}\nabla P_2^h \cdot \boldsymbol{n} - \int_{\Omega_2} f_2. \tag{15}$$

The quantity θ is not equal to zero in general and depends on the mesh size and the method used. From the definition of the scheme and the bilinear forms for CG-DG and DG-DG methods, we obtain the same expression for the mass balance for both methods. It is given below for the CG-DG and DG-DG methods:

$$\theta = -\sum_{e\in\Gamma_{2\mathrm{D}}} \frac{\sigma_e}{|e|} \int_e P_2^h + \int_{\Gamma_{2\mathrm{N}}} (g_{\mathrm{N}} - \boldsymbol{K}\nabla P_2^h \cdot \boldsymbol{n}) \tag{16}$$

However the quantities differ as they depend on the pressure approximation. From the expressions above, we can prove that θ converges to zero as h tends to zero, with a rate equal to $\mathcal{O}(h^{\min(k_1,k_2)-\frac{1}{2}})$ for the non-symmetric DG formulation and a rate equal to $\mathcal{O}(h^{\min(k_1,k_2)})$ with the symmetric DG formulation. For the CG-CG method, the expression for the mass balance is not as simple. This is due to the fact that the test functions for the Darcy pressure space vanish on the Dirichlet boundary $\Gamma_{2\mathrm{D}}$. Let $\varphi \in M^h$ be a continuous piecewise polynomial that takes the value zero for the constrained nodes on $\Gamma_{2\mathrm{D}}$ and the value one for all the free nodes. Let $\mathcal{S}$ be the union of mesh elements that share a vertex or an edge with $\Gamma_{2\mathrm{D}}$. Under the assumption that $\overline{\Gamma_{2\mathrm{D}}} \cap \overline{\Gamma_{12}} = \emptyset$, we can write for the CG-CG method:

$$\begin{aligned} \theta = &- \int_{\Gamma_{2\mathrm{N}}} (\boldsymbol{K} \nabla P_2^h - g_{\mathrm{N}} \varphi) - \int_{\mathcal{S}} f_2 (1 - \varphi) \\ &- \int_{\Gamma_{2\mathrm{D}}} \boldsymbol{K} \nabla P_2^h \cdot \boldsymbol{n} - \int_{\mathcal{S}} \boldsymbol{K} \nabla P_2^h \cdot \nabla \varphi. \end{aligned} \tag{17}$$

Quantifying θ for the coupled flow problem is important in the application to the filter problem described in the next section.

5.2 Filter problem

The coupling phenomenon that has been discussed in this work can also be found in industrial filtration systems. In [3], a coupled Stokes/Darcy model is proposed for industrial filtration systems and solved by using a mixed finite element method. Filtration systems play an important role in chemical and pharmaceutical industries in solid-liquid or solid-gas separations. We apply all three methods to the filtration problem described in [3]. The computational

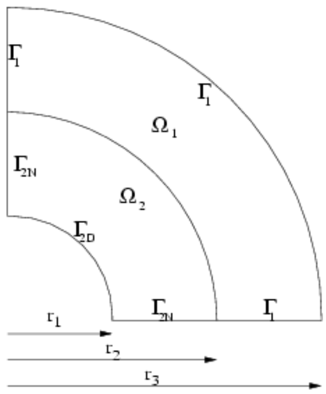

Fig. 12. Computational domain of a filtration problem.

domain is a concentric quarter circular divided into the porous and free flow media domains as shown in Fig. 5.2. The radii are $r_1 = 1, r_2 = 2, r_3 = 3$. The Navier-Stokes domain is partitioned into 1235 triangular elements and the Darcy domain into 726 triangular elements. We impose $\boldsymbol{u}_1 = (-x/30, -y/30)$ on the circular part of circular part of Γ_1 and $\boldsymbol{u}_1 = (0, -1)$, $\boldsymbol{u}_1 = (-1, 0)$ on the vertical and horizontal segments of Γ_1 respectively. We impose zero Dirichlet and Neumann boundary conditions for the Darcy pressure on $\Gamma_{2\mathrm{D}}$ and $\Gamma_{2\mathrm{N}}$ respectively. The input data is: $\boldsymbol{f}_1 = \boldsymbol{0}$, $f_2 = 0$, $\nu = 1$, $\alpha = 0.1$, $\delta = 10^{-6}$.

The low permeability in the porous medium causes pressure to build up during the filtration process. The life span of filtration equipment is heavily dependent on the hydrostatic pressure gradient that develops across the porous medium during filtration, as a result it is important to develop efficient models to determine the pressure gradient before any experiments are done [3]. Mass conservation is an important property of any numerical model that effectively simulates the filtration process.

First, we assume that the intrinsic permeability in the porous medium is equal to $10^{-7}\boldsymbol{I}$. Fig. 13 shows the numerical solutions obtained with the DG-DG scheme defined by the following parameters: $\epsilon_1 = \epsilon_2 = 1$, $\sigma_e = 0$ and $k_1 = k_2 = 2$. The solution converges with 4 Picard iterations. Fig. 14 is a plot

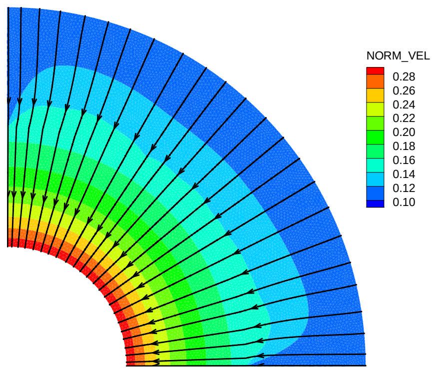

(a) Streamlines and velocity norm

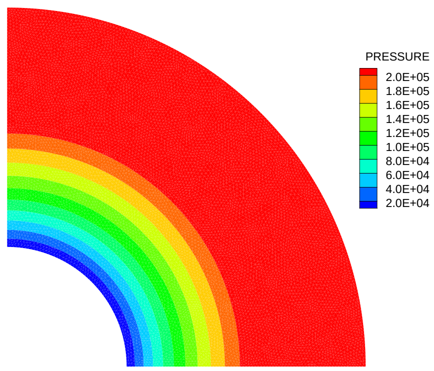

(b) Pressure

Fig. 13. Dead-end filter with permeability $\boldsymbol{k} = 10^{-7}\boldsymbol{I}$: DG-DG solution with $(k_1, k_2) = (2, 2)$.

of the solution obtained from the CG-DG scheme approximating the Darcy pressure with discontinuous quadratics with $\epsilon_2 = 1$, $\sigma_e = 0$. The flow characteristics of the solution from the CG-DG and DG-DG schemes are very similar and consistent with results obtained in [3] in which they observe a maximum

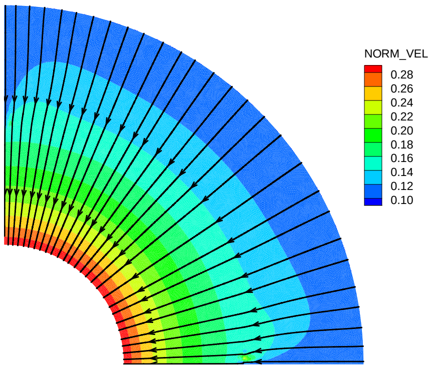

(a) Streamlines and velocity norm

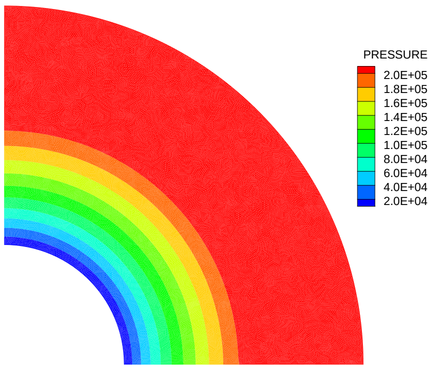

(b) Pressure

Fig. 14. Dead-end filter with permeability $\boldsymbol{k} = 10^{-7}\boldsymbol{I}$: CG-DG solution with $(k_1, k_2) = (1, 2)$.

pressure drop in the Darcy region. Table 8 shows the mass balance quantity $|\theta|$, computed by (15), for all three methods with different orders. The mesh of size h_0 is obtained by uniformly refining the mesh of size h_1. The inflow mass is:

$$\int_{\Gamma_1} \boldsymbol{U}^h \cdot \boldsymbol{n} = -0.471.$$

We first observe that smaller mass losses are obtained if the DG method with zero penalty is used in the Darcy region. Since the DG method with zero penalty is not stable for piecewise linear approximation, the polynomial degree has to be greater than or equal to two. We also note that adding the penalty increases the mass balance, which is expected from the expression (16). The mass balance for the CG-DG solution is smaller than the one obtained for the CG-CG solution. As we refine the mesh, the mass error decreases. The numerical rates correspond to the theoretical rates for both CG-DG and DG-DG methods. Indeed the rate is $\mathcal{O}(h^{3/2})$ for the DG-DG method of order two and it is $\mathcal{O}(h^{1/2})$ for the CG-DG method of order one. For the DG-DG method of order one, the numerical rate is $\mathcal{O}(h)$, which is a consequence to the usually observed optimal rate in the L^2 norm for the solution for odd polynomial degrees. However, on general meshes, one can only prove $\mathcal{O}(h^{1/2})$.

Method	k_1	k_2	σ_e	$\|\theta\|$ $(h = h_0)$	$\|\theta\|$ $(h = h_1)$	Rate
DG-DG	2	2	0	7.05×10^{-4}	2.64×10^{-4}	1.42
DG-DG	2	2	1	3.07×10^{-3}	1.47×10^{-3}	1.06
DG-DG	1	1	1	2.10×10^{-2}	1.06×10^{-2}	0.98
CG-DG	1	1	1	1.40×10^{-2}	1.08×10^{-2}	0.37
CG-DG	1	2	1	1.13×10^{-2}	8.56×10^{-3}	0.40
CG-DG	1	2	0	8.30×10^{-3}	6.20×10^{-3}	0.42
CG-CG	1	1	-	2.30×10^{-2}	1.45×10^{-2}	0.66

Table 8
Mass balance for filter problem.

Finally, Fig. 15 shows the solution obtained with the CG-CG scheme of order one. It is clear that the solution obtained from the DG-DG scheme results in greater conservation of mass compared to the other scheme. The dead-end filtration systems simulated in work by Hanspal *et al.* [3] have permeability in the range of 10^{-12} to 10^{-14}. We next test the DG-DG schem with permeability equal to 10^{-12}. The mass loss is equal to $7.23e-4$.

Fig. 16 shows the solution obtained from a porous medium with permeability equal to 10^{-12}. As expected the lower permeability in the porous medium results in a build up of pressure higher than shown in Fig. 13 and Fig. 14 obtained from a porous medium with permeability equal to 10^{-7}. From this simulation we can conclude that the DG-DG scheme of order two performs better in problems in which mass conservation is an important component.

6 Conclusion

Three numerical methods are employed for solving the coupled problem of Navier-Stokes and Darcy flows. The first method, refered as the CG-CG method, uses continuous finite element methods in the whole domain, which yields the smaller size problem on a given mesh. The second method, refered as the DG-DG method uses discontinuous Galerkin method in the whole domain, which is a robust scheme for heterogeneous media. Finally the third method, refered as the CG-DG method, combines the finite element method for the Navier-Stokes region with the discontinuous Galerkin method for the

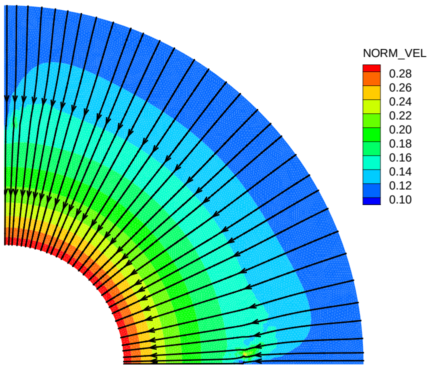

(a) Streamlines and velocity norm

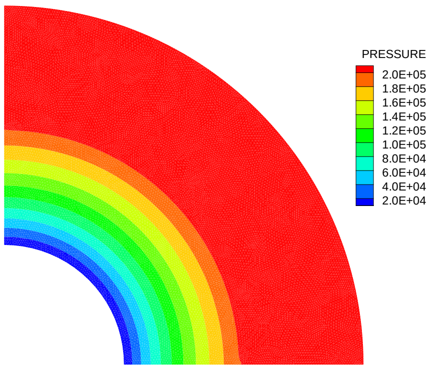

(b) Pressure

Fig. 15. Dead-end filter with permeability $\boldsymbol{k} = 10^{-7}\boldsymbol{I}$: CG-CG solution with $(k_1, k_2) = (1, 1)$.

Darcy region. Each method captures the essential features of the flow for the examples considered in this paper. However increasing the order of approximation in the Darcy region has a direct impact on the accuracy of the overall solution. To that effect, we recommend to use the CG-DG scheme with order one elements in the free flow region and order two elements in the porous medium. This yields a robust and accurate method with manageable problem size. We also show that the numerical mass loss in the DG-DG scheme with zero penalty is significantly less than the numerical mass loss in the CG-DG or CG-CG schemes. If mass conservation is an important feature of the problem at hand, then the DG-DG method is the most appropriate one.

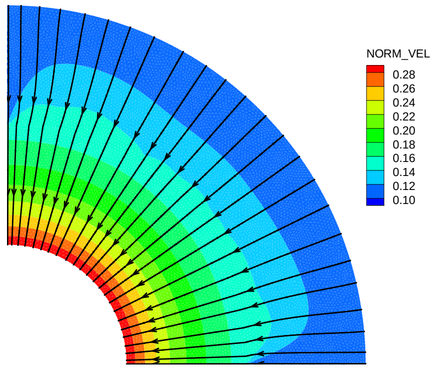

(a) Streamlines and velocity norm

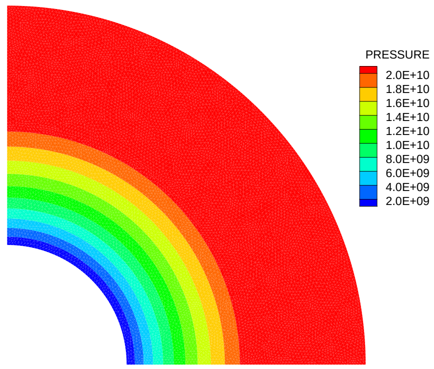

(b) Pressure

Fig. 16. Dead-end filter with permeability $\boldsymbol{k} = 10^{-12}\boldsymbol{I}$: DG-DG solution with $(k_1, k_2) = (2, 2)$.

References

[1] A. Salinger, R. Aris, J. Derby, Finite element formulations for large-scale coupled flows in adjacent porous and open fluid domains, International Journal for Numerical Methods in Fluids 18 (1994) 1185–1209.

[2] V. Nassehi, Modelling of combined Navier-Stokes and Darcy flows in crossflow membrane filtration, Chemical Engineering Science 53 (6) (1998) 1253–1265.

[3] N. Hanspal, A. Waghode, V. Nassehi, R. Wakeman, Numerical analysis of coupled Stokes/Darcy flows in industrial filtrations, Transport in Porous Media 64 (1) (2006) 73–101.

[4] M. Discacciati, A. Quarteroni, Analysis of a domain decomposition method for the coupling of Stokes and Darcy equations, in: B. et al (Ed.), Numerical Analysis and Advanced Applications - ENUMATH 2001, Springer, Milan, 2003, pp. 3–20.

[5] M. Discacciati, E. Miglio, A. Quarteroni, Mathematical and numerical models for coupling surface and groundwater flows, Appl. Numer. Math. 43 (2001) 57–74.

[6] W. Layton, F. Schieweck, I. Yotov, Coupling fluid flow with porous media flow, SIAM J. Numer. Anal. 40 (6) (2003) 2195–2218.

[7] B. Rivière, I. Yotov, Locally conservative coupling of Stokes and Darcy flow, SIAM J. Numer. Anal. 42 (2005) 1959–1977.

[8] B. Rivière, Analysis of a discontinuous finite element method for the coupled Stokes and Darcy problems, Journal of Scientific Computing 22 (2005) 479–500.

[9] B. Rivière, Analysis of a multi-numerics/multi-physics problem, Numerical Mathematics and Advanced Applications (2004) 726–735.

[10] M. Discacciati, A. Quarteroni, A. Valli, Robin-Robin domain decomposition methods for the Stokes-Darcy coupling, SIAM J. Numer. Anal. 45 (3) (2007) 1246–1268.

[11] E. Burman, P. Hansbo, A unified stabilized method for Stokes and Darcy's equations, J. Computational and Applied Mathematics 198 (1) (2007) 35–51.

[12] L. Badea, M. Discacciati, A. Quarteroni, Mathematical analysis of the Navier-Stokes and Darcy coupling, Technical Report of Politecnico di Milano.

[13] V. Girault, B. Rivière, DG approximation of coupled Navier-Stokes and Darcy equations by Beaver-Joseph Saffman interface condition, SIAM Journal on Numerical Analysis 47 (2009) 2052–2089.

[14] P. Chidyagwai, B. Rivière, On the solution of the coupled Navier-Stokes and Darcy equations, Computer Methods in Applied Mechanics and Engineering. 198 (2009) 3806–3820.

[15] A. Cesmelioglu, B. Rivière, Analysis of time-dependent Navier-Stokes flow coupled with Darcy flow, Journal of Numerical Mathematics 16 (4) (2008) 249–280.

[16] M. Discacciati, Domain decomposition methods for the coupling of surface and groundwater flows, Ph.D. thesis, Ecole Polytechnique Fédérale de Lausanne, Switzerland (2004).

[17] A. Cesmelioglu, B. Rivière, Primal discontinuous Galerkin methods for time-dependent coupled surface and subsurface flow, Journal of Scientific Computing 40 (2009) 115–140.

[18] G. Beavers, D. Joseph, Boundary conditions at a naturally permeable wall, Journal of Fluid Mechanics 30 (1967) 197–207.

[19] P. Saffman, On the boundary condition at the surface of a porous medium, Journal of Fluid Mechanics 2 (1971) 93–101.

[20] W. Jager, A. Mikelic, N. Neuss, Asymptotic analysis of the laminar viscous flow over a porous bed, SIAM Journal on Scientific Computing 22 (2001) 2006–2028.

[21] D. Arnold, F.Brezzi, M. Fortin, A stable finite element for the Stokes equations, Calcolo 21 (4) (1984) 337–344.

[22] C.Taylor, P.Hood, A numerical solution of the Navier-Stokes equations using the finite element technique, Computers & Fluids 1 (1973) 73–100.

[23] S. C. Brenner, L. R. Scott, The Mathematical Theory of Finite Element Methods, Springer, 2007, third Edition.

[24] V. Girault, B. Rivière, M. Wheeler, A Discontinuous Galerkin Method with Non-Overlapping Domain Decomposition for the Stokes and Navier-Stokes Problems, Mathematics of Computation 74 (2005) 53–84.

[25] E. Kaasschieter, Mixed finite elements for accurate particle tracking in saturated groundwater flow, Advances in Water Resources 18 (5) (1995) 277–294.

[26] Y. Epshteyn, B. Rivière, Estimation of penalty parameters for symmetric interior penalty Galerkin methods, Journal of Computational and Applied Mathematics 206 (2007) 843–872.